Advanced Electronic Materials

ADVANCED ELECTRONIC MATERIALS Open Access

www.advelectronicmat.de

RESEARCH ARTICLE OPEN ACCESS

Discovery of an Ideal HgO_{12} Icosahedron and Magnetodielectric Coupling in $HgCu_3Ti_4O_{12}$

Haoyu Zheng[1,2] | Jianfa Zhao[2] | Jun Deng[3] | Lei Duan[1] | Xudong Shen[4] | Zhiwei Hu[5] | Luchuan Shi[2] | Yuling Dai[2] | Xiaoming Chen[1,2] | Xubin Ye[2] | Jun Zhang[2] | Wenmin Li[6] | Zheng Deng[2] | Xiancheng Wang[2,7] | Chang-Yang Kuo[8,9] | Chien-Te Chen[8] | Youwen Long[2,7] | Runze Yu[3] | Changjiang Xiao[1] | Changqing Jin[2,7]

[1]School of Material Science and Engineering, Henan University of Technology, Zhengzhou, China | [2]Beijing National Laboratory For Condensed Matter Physics, Institute of Physics, Chinese Academy of Sciences, Beijing, China | [3]Center For High-Pressure Science and Technology Advanced Research, Beijing, China | [4]Spallat Neutron Source Sci Ctr, Institute of High Energy Physics, Chinese Academy of Science, Beijing, China | [5]Max-Planck Institute for Chemical Physics of Solids, Dresden, Germany | [6]Institute of Quantum Materials and Physics, Henan Academy of Sciences, Zhengzhou, China | [7]School of Physical Sciences, University of Chinese Academy of Sciences, Beijing, China | [8]National Synchrotron Radiation Research Center, Hsinchu Science Park, Hsinchu, Taiwan (ROC) | [9]Department of Electrophysics, National Yang Ming Chiao Tung University, Hsinchu, Taiwan (ROC)

Correspondence: Jianfa Zhao (zhaojf@iphy.ac.cn) | Jun Deng (jun.deng@hpstar.ac.cn) | Changjiang Xiao (cjxiao@haut.edu.cn) | Changqing Jin (jin@iphy.ac.cn)

Received: 10 February 2026 | **Revised:** 27 April 2026 | **Accepted:** 25 May 2026

ABSTRACT

We report the first successful high-pressure synthesis and comprehensive characterization of A-site-ordered quadruple perovskite $HgCu_3Ti_4O_{12}$. The compound crystallizes in the cubic *Im*-3 structure with $Hg^{2+}Cu^{2+}{}_3Ti^{4+}{}_4O^{2-}{}_{12}$ valence configuration. A remarkable structural feature is the observation of a perfectly regular and undistorted HgO_{12} icosahedron, representing the highest and most symmetric oxygen coordination environment reported for Hg^{2+} in any oxide material. Magnetic and specific heat measurements reveal the antiferromagnetic ordering at $T_N = 31$ K, driven by indirect super-exchange interaction via the Cu^{2+}-O^{2-}-Ti^{4+}-O^{2-}-Cu^{2+} pathway. The dielectric properties of $HgCu_3Ti_4O_{12}$ display a significantly lower, more intrinsic permittivity ($\sim 10^2$) with two distinct Debye-type relaxation processes: a high-temperature process related to oxygen vacancy–defect dipole reorientation, and a low-temperature process attributed to low-energy local lattice vibrations of the TiO_6 or CuO_4 units. Crucially, a dielectric anomaly around T_N suggests the presence of magnetodielectric coupling, likely mediated by the aforementioned indirect super-exchange interaction pathway. This work elucidates the structure–property relationships in $HgCu_3Ti_4O_{12}$, highlights the critical role of cation chemistry in tailoring functional properties, and demonstrates the potential of A-site-ordered quadruple perovskites as a versatile platform for exploring coupled electronic, magnetic, and dielectric phenomena.

1 | Introduction

Perovskites and their derivatives show many interesting performances [1, 2]. Especially, A-site-ordered quadruple perovskites with the general chemical formula $AA'_3B_4O_{12}$ have emerged as a highly prominent class of materials in condensed matter physics and materials science, drawing significant and widespread attention due to their extraordinary structural architecture and the remarkably diverse spectrum of fascinating physical properties they exhibit [3]. These compounds usually crystallize in a cubic structure with the space group *Im*-3 (No.204), wherein the conventional single 12-coordinated A-site of the simple ABO_3 perovskite is reconfigured into a 1:3 ordered arrangement. Specifically, the A-site, typically occupied by rare-earth, alkaline-earth,

Haoyu Zheng and Jianfa Zhao contributed equally to this work.

or alkali-metal ions, forms an icosahedral AO_{12} coordination environment, while the A′-site is occupied by transition-metal ions with a smaller ionic radius, most commonly Jahn–Teller active ions such as Cu^{2+} and Mn^{3+}, which reside in a distinctive square-planar $A'O_4$ coordination. The B-site is also filled by transition-metal ions, forming a network of corner-sharing BO_6 octahedra. A critical structural consequence of this unique cation ordering is the substitution of three-quarters of the original perovskite A-sites with smaller transition-metal cations, which forces a significant tilting of the BO_6 octahedra (with B—O—B bond angles typically around 140°) [4]. This pronounced distortion often necessitates high-pressure synthesis conditions to stabilize the overall $AA'_3B_4O_{12}$ perovskite framework. The core scientific interest in these materials stems from the coexistence of transition-metal ions at both the A′ and B lattice sites. This configuration enables a rich interplay of multiple magnetic and electronic interactions—including A′-A′, B-B, and, most notably, A′-B interactions—that are absent in conventional perovskites [5]. This complex interaction landscape gives rise to an exceptional array of emergent phenomena. Documented properties include giant dielectric constants over wide temperature ranges [6], various magnetic transitions (ferromagnetic, ferrimagnetic, and antiferromagnetic) [7, 8], multiferroicity [9], and large ferroelectric polarization [10]. Therefore, $AA'_3B_4O_{12}$ quadruple perovskites represent a versatile and unparalleled platform for investigating the profound effects of coordination geometry, cation ordering, and complex inter-site correlations on fundamental material properties, driving continuous exploration for novel quantum states and functional applications.

Over the past few decades, titanium-based A-site-ordered quadruple perovskites with the general formula $AA'_3B_4O_{12}$ have attracted significant research attention owing to their remarkable dielectric and ferroelectric properties, which hold considerable promise for applications in advanced electronic devices such as supercapacitors and room-temperature ferroelectric memories [6, 11–14]. A prominent example is $CaCu_3Ti_4O_{12}$, which exhibits an exceptionally high dielectric constant ($\varepsilon' \sim 10^4$–10^5) across broad temperature (100–600 K) and frequency (1 Hz–10 MHz) ranges [15–18]. These characteristics make it highly suitable for use in microelectronic bypass capacitors and energy-storage components [19]. More recently, another member of this structural family, $PbHg_3Ti_4O_{12}$, was successfully synthesized under high-pressure conditions [3]. This compound undergoes a phase transition from a high-temperature centrosymmetric cubic paraelectric state to a low-temperature non-centrosymmetric orthorhombic ferroelectric phase, displaying a record high Curie temperature ($T_c \sim 250$ K) among known A-site-ordered quadruple perovskites. Theoretical and experimental analyses indicate that the ferroelectric distortion in $PbHg_3Ti_4O_{12}$ is primarily driven by anomalies in Ti—O phonon modes. The discovery of $PbHg_3Ti_4O_{12}$ not only suggests a viable route for designing high-T_c ferroelectric materials within this perovskite family but also reinforces the potential of such compounds for practical applications in capacitive energy storage and non-volatile memory devices.

Inspired by these advances and recognizing the vast compositional flexibility of the $AA'_3B_4O_{12}$ structure, we turned our attention to another promising yet unexplored combination: $HgCu_3Ti_4O_{12}$. In this work, we report the first successful synthesis of polycrystalline $HgCu_3Ti_4O_{12}$ under high-pressure and high-temperature conditions. A comprehensive investigation of its structural and physical properties was carried out to understand how the substitution of A/A′ site cations influences the material's behavior. X-ray diffraction and refinement were employed to determine the crystal structure and phase purity. The charge state and electronic environment of constituent ions were probed using X-ray absorption spectroscopy. Magnetic susceptibility and specific heat measurements were conducted to examine possible magnetic ordering or interactions originating from the Cu^{2+} ions at the A′-site. Finally, frequency- and temperature-dependent dielectric spectroscopy was used to characterize the permittivity, loss tangent, and possible ferroelectric responses. Through this multi-faceted study, we aim to elucidate the structure–property relationships in $HgCu_3Ti_4O_{12}$, assess its functional potential, and contribute to the broader understanding of the role of cation chemistry in tailoring the dielectric and ferroelectric performance of A-site-ordered quadruple perovskites.

2 | Results and Discussion

XRD patterns collected at room temperature and Rietveld structural refinement results for $HgCu_3Ti_4O_{12}$ are shown in Figure 1a. The refinement confirms that the compound crystallizes in the A-site-ordered quadruple perovskite structure with the $AA'_3B_4O_{12}$ stoichiometry and adopts the space group *Im*-3(No.204), making it isostructural with $CaCu_3Ti_4O_{12}$. In this symmetry, Hg and Cu atoms are arranged in a 1:3 order at the specific Wyckoff sites 2*a* (0, 0, 0) and 6*b* (0, 0.5, 0.5), respectively. The B-site Ti atoms are situated at the 8*c* position (0.25, 0.25, 0.25), forming a network of corner-sharing TiO_6 octahedra, and the oxygen atoms reside at the general 24 *g* site (0, y, z). A schematic representation of the crystal structure is shown in Figure 1b. A notable feature is the square-planar coordination of the A′-site Cu atoms (CuO_4), which arises from the Jahn–Teller distortion and contrasts sharply with the 12-coordinate environment of the A-site Hg atoms. The detailed refined structural parameters, including lattice constants, atomic coordinates, selected bond lengths, and bond angles, are summarized in Table 1. Bond-valence-sum (BVS) calculations [20], using the standard bond-valence relation $V_i = \sum_j S_{ij}$, yielded values of +1.99 for Cu, and +3.90 for Ti. These results support a charge distribution of $Hg^{2+}Cu^{2+}{}_3Ti^{4+}{}_4O_{12}$, a conclusion further corroborated by subsequent *s*XAS measurements. Figure 1c,d highlights the unique polyhedral geometry around Hg in $HgCu_3Ti_4O_{12}$ when compared to other mercury-containing oxides such as $HgTiO_3$[21], monoclinic and rhombohedral $HgMnO_3$[22], $PbHg_3Ti_4O_{12}$[3], and $(Hg_{0.75}Pb_{0.25})MnO_3$[23]. In most of these compounds, significant variation in the Hg—O bond lengths within a single coordination polyhedron leads to pronounced distortion of the HgO_x polyhedron. By contrast, in $HgCu_3Ti_4O_{12}$, all twelve Hg—O bonds are equivalent, resulting in a perfectly regular, undistorted HgO_{12} polyhedron. This difference is quantified using the distortion parameter Δ, defined as $\Delta = \frac{1}{x}\sum_{i=1}^{x}\left(\frac{d_i - d_{av}}{d_{av}}\right)^2$, where d_i are individual bond lengths, and d_{av} is their average [23, 24]. As seen in Figure 1d, Δ for $HgCu_3Ti_4O_{12}$ is effectively zero, while values for typical mercury oxides are considerably higher. Moreover, in representative reported Hg-based oxides, such as $HgTiO_3$, monoclinic and rhombohedral $HgMnO_3$, $PbHg_3Ti_4O_{12}$, and $(Hg_{0.75}Pb_{0.25})MnO_3$, Hg^{2+} usually adopts lower

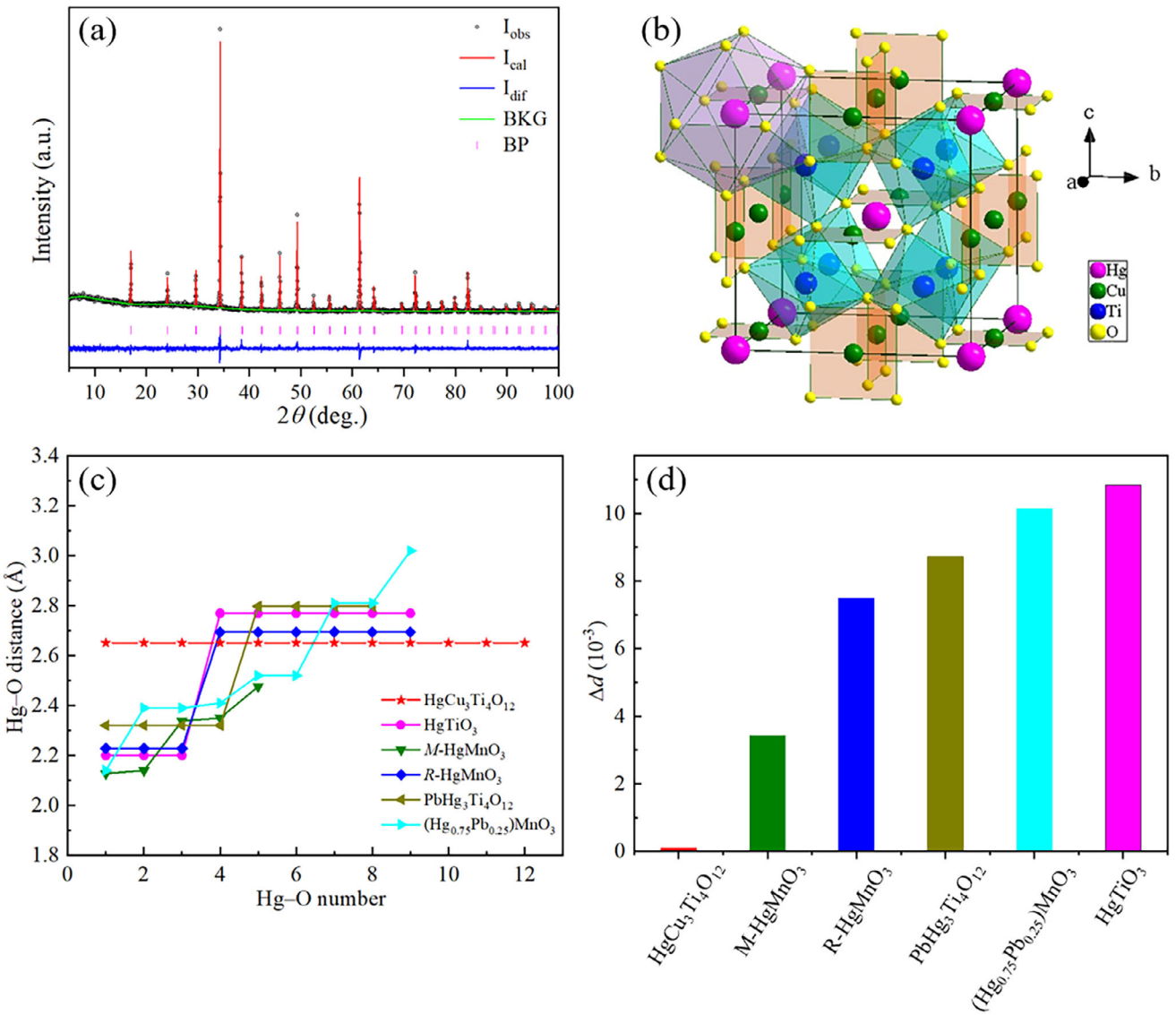

FIGURE 1 | (a) XRD Rietveld structural refinement results for $HgCu_3Ti_4O_{12}$ collected at room temperature. Observed (circle), calculated (red line), and difference (blue line) were shown, respectively. The vertical bar with magenta color indicates the allowed Bragg reflections; (b)The crystal structure of $HgCu_3Ti_4O_{12}$; (c) Comparison of the A-site Hg—O bond lengths for $HgCu_3Ti_4O_{12}$ as well as $HgTiO_3$[21], *M*-$HgMnO_3$[22], *R*-$HgMnO_3$[22], $PbHg_3Ti_4O_{12}$[3], and $(Hg_{0.75}Pb_{0.25})MnO_3$[23]; (d) Comparison of HgO_x polyhedral distortion parameter (Δd) for the $HgCu_3Ti_4O_{12}$ as well as $HgTiO_3$[21], *M*-$HgMnO_3$[22], *R*-$HgMnO_3$[22], $PbHg_3Ti_4O_{12}$[3], and $(Hg_{0.75}Pb_{0.25})MnO_3$[23].

or significantly distorted oxygen coordination environments, with effective coordination numbers typically not exceeding eight [3, 21–23]. The observation of 12-coordinate Hg in $HgCu_3Ti_4O_{12}$, coupled with its complete absence of polyhedral distortion, is therefore exceptional. To our knowledge, this represents the first report of such a high and symmetric oxygen coordination environment for mercury in any oxide material, underscoring the distinctive structural chemistry stabilized within this quadruple perovskite framework.

The energy position and multiplet spectral features of *s*XAS at the 3*d* elements $L_{2,3}$-edges are highly sensitive to the valence states and local environment of cations [25–28]. To precisely determine the oxidation states of Cu and Ti ions in $HgCu_3Ti_4O_{12}$, the Cu $L_{2,3}$ and Ti $L_{2,3}$-edges sXAS spectra were measured. Figure 2a shows the sXAS spectra at the Ti $L_{2,3}$-edges of $HgCu_3Ti_4O_{12}$ together with $CaCu_3Ti^{4+}{}_4O_{12}$ and $SrTi^{4+}O_3$ as Ti^{4+} reference. The same energy position and very similar multiplet spectral feature (four main peaks and two weak pre-edge peaks) for $HgCu_3Ti_4O_{12}$, $CaCu_3Ti_4O_{12}$, and $SrTiO_3$ indicate the same Ti^{4+} valence state in those compounds [26, 29]. The detailed multiplet spectral shape of $HgCu_3Ti_4O_{12}$ is similar to that of $CaCu_3Ti_4O_{12}$, as compared with that of $SrTiO_3$, indicating a very similar local environment for the former two. (In fact, there are seven transitions for the $3d^0$ ground state in octahedral coordination. A line located between t_{2g} peak and e_g peak at the L_3-edge is not solved, resulting in an asymmetry peak at the L_3-edge) [26]. Figure 2b shows the Cu $L_{2,3}$-edge sXAS of $HgCu_3Ti_4O_{12}$ together with $CaCu^{2+}{}_3Ti_4O_{12}$ and $Cu^{2+}O$ as Cu^{2+} reference [30]. One can find that the energy positions of the single symmetry peak in $HgCu_3Ti_4O_{12}$ closely resemble those of $CaCu^{2+}{}_3Ti_4O_{12}$ and $Cu^{2+}O$, indicating the presence of Cu^{2+} in $HgCu_3Ti_4O_{12}$ [31]. The sXAS results confirm the oxidation states

TABLE 1 | Rietveld Refinement Results for $HgCu_3Ti_4O_{12}$ at 300 K.

	$HgCu_3Ti_4O_{12}$
a(Å)	7.4052(9)
Z	2
Formula weight (g/mol)	774.73
Calc. Density (g/cm^3)	6.337
V(Å^3)	406.09(4)
O_x	0
O_y	0.6902(1)
O_z	0.1795(0)
U_{iso}(Hg)(100×Å^2)	3.79(9)
U_{iso}(Cu)(100×Å^2)	4.07(9)
U_{iso}(Ti)(100×Å^2)	3.95(5)
U_{iso}(O)(100×Å^2)	4.18(0)
Hg-O(×12)(Å)	2.6513(8)
Cu-O(×4)(Å)	1.9367(6)
Ti-O(×6)(Å)	1.9738(2)
∠Ti-O-Ti (°)	139.417(0)
BVS(Hg)	1.91
BVS(Cu)	1.99
BVS(Ti)	3.90
R_{wp}(%)	8.41
R_p(%)	6.54

Space group: *Im*-3. Atomic sites: Hg 2*a* (0, 0, 0), Cu 6*b* (0, 0.5, 0.5), Ti 8*c* (0.25, 0.25, 0.25), and O 24 *g* (0, *y*, *z*). The BVS values (V_i) were calculated via the formula $V_i = \sum_j S_{ij}$, where $S_{ij} = \exp[(r_0 - r_{ij})/0.37]$ using parameters $r_0(Hg^{2+}) = 1.972$ Å, $r_0(Cu^{2+}) = 1.679$ Å, and $r_0(Ti^{4+}) = 1.815$ Å. 12-, 4-, and 6-coordinated oxygen atoms were utilized for the A-site Hg, A′-site Cu, and B-site Ti, respectively.

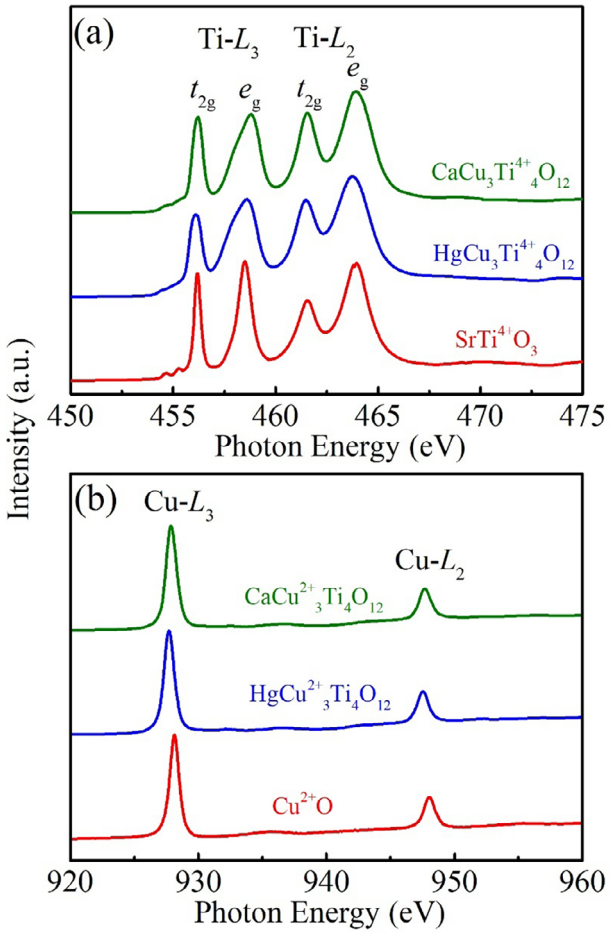

FIGURE 2 | (a) sXAS spectra of Ti-$L_{2,3}$ edges for $HgCu_3Ti_4O_{12}$, along with $CaCu_3Ti^{4+}{}_4O_{12}$ and $SrTi^{4+}O_3$ as the Ti^{4+} reference. (b) sXAS spectra of Cu-$L_{2,3}$ edges for $HgCu_3Ti_4O_{12}$ along with $CaCu^{2+}{}_3Ti_4O_{12}$ and $Cu^{2+}O$ as the Cu^{2+} reference.

of $Hg^{2+}Cu^{2+}{}_3Ti^{4+}{}_4O^{2-}{}_{12}$, which is consistent with the BVS results mentioned above.

The temperature dependence of magnetic susceptibility (M–T) for $HgCu_3Ti_4O_{12}$ is shown in Figure 3a. The antiferromagnetic (AFM) order is observed with Neel temperature (T_N) of 31 K for $HgCu_3Ti_4O_{12}$, which is similar to the homologous compounds $ACu_3Ti_4O_{12}$ (A = Ca, Sr, Cd). Figure 3b shows the field dependence of magnetization (M–H) measured at different temperatures. The magnetization is linearly dependent on the applied magnetic field, and no open magnetic hysteresis loop was observed in $HgCu_3Ti_4O_{12}$ below T_N, indicating a simple *G*-type collinear AFM structure similar to that of $CaCu_3Ti_4O_{12}$ [32, 33]. The magnetic susceptibility above the transition temperature can be well fitted with the Curie-Weiss law, $\chi(T) = C/(T - \theta_w)$, where *C* is the Curie constant and θ_w is the Weiss temperature. The obtained Curie constant is $C = 1.50$ emu K mol^{-1} Oe^{-1}, and the Weiss temperature is $\theta_w = -40.2$ K for $HgCu_3Ti_4O_{12}$, confirming the AFM interactions. Since the valence state of $HgCu_3Ti_4O_{12}$ is $Hg^{2+}Cu^{2+}{}_3Ti^{4+}{}_4O_{12}$, only the Cu^{2+} ions with $3d^9$ configuration carry a local moment. Ti^{4+} and Hg^{2+}, respectively, have $3d^0$ and $5d^{10}$ configurations and thus exhibit no magnetic moment. According to the Curie constant, the effective magnetic moment (μ_{eff}) was estimated using $\mu_{eff} = (8C/3)^{1/2}\mu_B$ and was calculated to be 2.00 μ_B / Cu^{2+} for $HgCu_3Ti_4O_{12}$. This μ_{eff} value is slightly higher than the spin-only theoretical value (1.73 μ_B) for the Cu^{2+} ion with $S = 1/2$, and it corresponds to the enhanced *g*-value of 2.31. The similar deviations were also observed in $CaCu_3Ti_4O_{12}$ (μ_{eff} = 1.9 μ_B/Cu) [33, 34] and $SrCu_3Ti_4O_{12}$ (μ_{eff} = 1.95–2.09 μ_B/Cu) [12, 32]. One reasonable explanation is that the spin-orbital coupling effect contributes to the AFM interaction between the Cu ions in $ACu_3Ti_4O_{12}$ (A = Ca, Sr, Cd, Hg) system [14].

According to the previous study, the magnetic structure of the $CaCu_3Ti_4O_{12}$ was described as the Cu^{2+} ordered collinearly along the crystallographic [111] direction [35]. The first and third nearest neighbor Cu^{2+} are antiferromagnetically correlated, while the interaction between the second neighbor Cu^{2+} is FM. Any direct exchange between Cu^{2+} ions is negligibly small due to the large distances between these ions. The indirect exchange interaction between the Cu^{2+} ions via Cu^{2+}-O^{2-}-Ti^{4+}-O^{2-}-Cu^{2+} pathway is believed to be most important [12]. Therefore, the intensity of super-exchange interaction between the Cu^{2+} in $ACu_3Ti_4O_{12}$ (A = Ca, Sr, Cd, Hg) system is dependent on Cu/Ti—O bond length and Cu—O—Ti angle. Table 2 summarizes ionic radius r_A, structural parameters, and T_N for the $ACu_3Ti_4O_{12}$ (A = Ca, Sr, Cd, Hg) system. The ionic radii r_A with 12-coordinated take

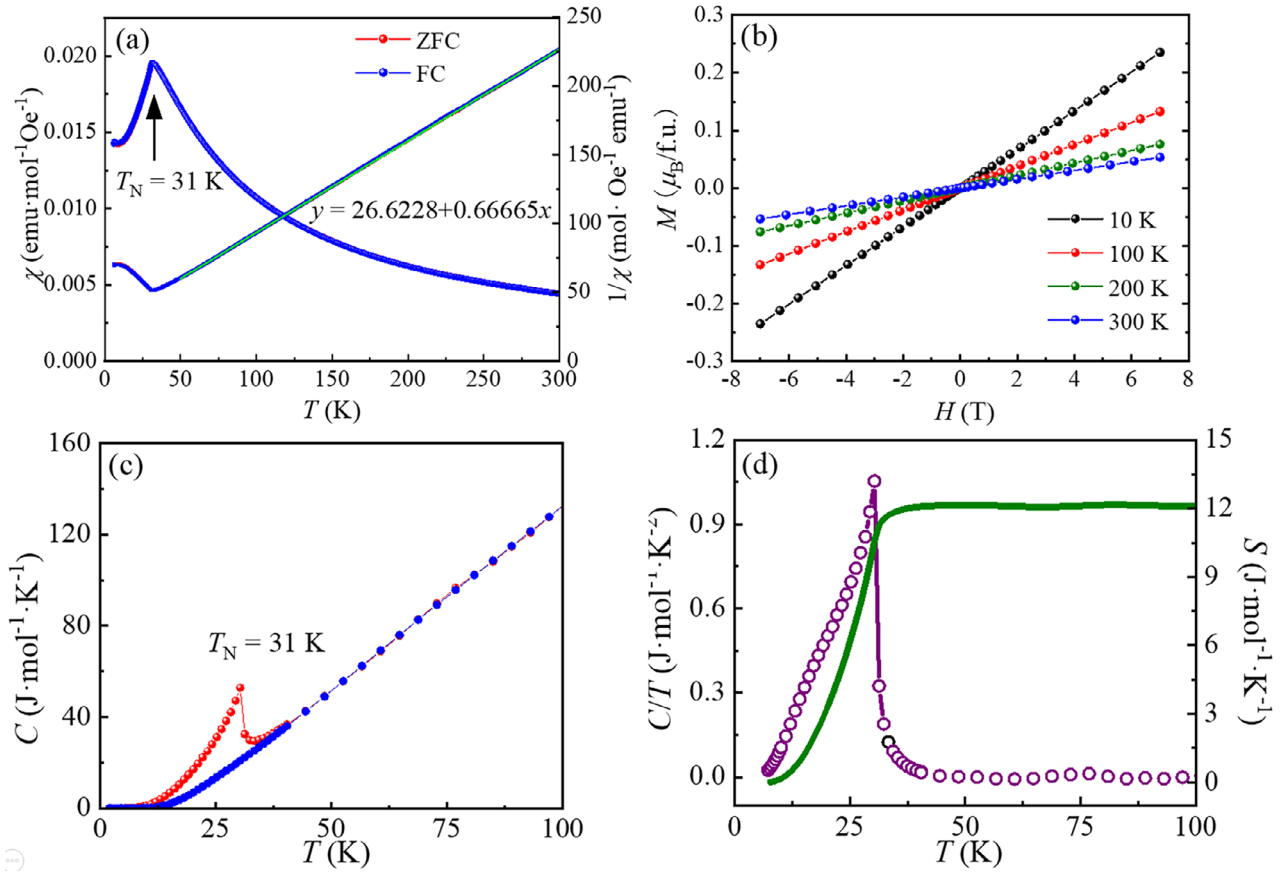

FIGURE 3 | (a) Temperature-dependent magnetic susceptibility χ measured under the field of 0.1 T using ZFC and FC modes, along with the inverse magnetic susceptibility, for $HgCu_3Ti_4O_{12}$. The green line indicates the Curie–Weiss fitting between 50 and 300 K; (b) Field-dependent magnetization for $HgCu_3Ti_4O_{12}$ collected at 10, 100, 200, and 300 K; (c) Temperature dependence of specific heat for $HgCu_3Ti_4O_{12}$. The blue curve shows the fit of lattice specific heat; (d) C_p/T vs. T and the numerical integration of the entropy S after subtracting the lattice specific heat around T_N for $HgCu_3Ti_4O_{12}$.

TABLE 2 | Ionic radius of A-site r_A, lattice constant a, A—O, Cu—O, Ti—O bond length, ∠Ti—O—Ti, ∠Cu—O—Ti, and T_N for $ACu_3Ti_4O_{12}$ (A = Ca, Sr, Cd, Hg) perovskite compounds [12, 37–39].

	$CaCu_3Ti_4O_{12}$	$SrCu_3Ti_4O_{12}$	$CdCu_3Ti_4O_{12}$	$HgCu_3Ti_4O_{12}$
r_A (Å)	1.34	1.44	1.31	—
a (Å)	7.4037	7.4278	7.3913	7.4052(9)
A-O (Å)	2.608(1)	2.6303	2.59465	2.6514
Cu-O (Å)	1.978(1)	1.9884	1.99195	1.93679
Ti-O (Å)	1.9625(4)	1.9653	1.95248	1.97381
∠ *Ti-O-Ti* (°)	141.33(6)	141.77	142.3112	139.4184
∠ *Cu-O-Ti* (°)	108.9774	108.8657	108.4625	110.1607
T_N (K)	25	24.5	29	31

from Shannon's Table [36]. Unfortunately, we could not obtain any value of Hg^{2+} with 12-coordinated oxygen since there is never observed such a high coordination number of Hg^{2+} has never been observed before. Nevertheless, it is noteworthy that although the A-site ionic radii r_A change significantly, eg, Sr^{2+} is 7.4% larger than Ca^{2+}, the structural changes do not follow a simple rigid-sphere ionic model. As shown in Table 2, the A—O and Cu—O bond lengths show noticeable variations with different A-site cations, whereas the lattice constants, Ti—O bond lengths, and ∠Ti—O—Ti/Cu—O—Ti bond angles remain within a relatively limited range. Correspondingly, the AFM transition temperatures remain close, ranging from 24.5 to 31 K. These results suggest that the *A*-site cage can accommodate cations of different sizes without inducing a drastic reconstruction of the CuO_4−TiO_6 framework or a pronounced change in the magnetic transition temperature. A similar phenomenon was also observed in the $ACu_3Sn_4O_{12}$ (*A* = Ca, Sr, Pb) series, where the difference in the size of the *A*-site ions has little effect on the ferromagnetic

transition temperatures [8]. All these observations imply that the size effect at the *A*-site cannot be explained by a simple rigid-sphere ionic model and that the cage structure at the *A*-site can accommodate ions of different sizes without significant structural and magnetic change [8].

Figure 3c shows the temperature dependence of specific heat for $HgCu_3Ti_4O_{12}$ without an external magnetic field, respectively. The sharp λ-type anomalies at 31 K support the transitions of long-range magnetic ordering in $HgCu_3Ti_4O_{12}$ [13]. In order to estimate the entropy release associated with AFM ordering, the lattice contribution has been calculated and subtracted from the total specific heat [40]. For this purpose, we fitted the lattice contribution with the Debye model, $C_{lat}(T) = 9nR(\frac{T}{\Theta_D})^3 \int_0^{\Theta_D/T} \frac{x^4 e^x}{(e^x-1)^2} dx$, where n is the number of atoms per formula unit, R is the gas constant, and Θ_D is the Debye temperature (blue curve in Figure 3c). Figure 3d shows C_p/T vs. T and the magnetic entropy $S_{mag} = \int_{T1}^{T2} (C_{mag}/T) dT$ for $HgCu_3Ti_4O_{12}$[40]. Magnetic entropy increases with temperature and nearly saturates just above T_N with the value of 12.06 J mol^{-1} K^{-1}. In $HgCu_3Ti_4O_{12}$, the Cu^{2+} ions carry a hole with spin $S = 1/2$ in the 3*d* shell. Therefore, the value of magnetic entropy is expected to be $3R^*\ln(2S + 1) =$ 17.28 J mol^{-1} K^{-1}. The experimental value is approximately 70% of the theoretical value, which is smaller than the full spin entropy expected for three Cu^{2+} ions. This reduced entropy may be attributed to partial magnetic entropy release above T_N associated with short-range magnetic correlations, as well as uncertainty in the lattice-background subtraction. Nevertheless, the clear λ-type anomaly in the specific heat supports the bulk nature of the AFM order in $HgCu_3Ti_4O_{12}$.

Given the brown color of polycrystalline $HgCu_3Ti_4O_{12}$, its optical properties were evaluated by UV–vis–NIR absorption spectroscopy (Figure 4a). Aside from a small vapor absorption feature at 1390 nm, the spectrum showed a steep decline as wavelength increased—a behavior typical of semiconductors. The optical band gap was estimated using the equation $(f(R)h\nu)^n = A(h\nu\text{-}E_g)$, where $f(R)$, h, ν, A, and E_g represent the Kubelka–Munk function, Planck's constant, light frequency, proportional constant, and band gap, and $n = 2$ or 1/2 depending on whether the transition is direct or indirect. Here, we chose $n = 1/2$ because the DFT band structure indicates an indirect band gap, as shown in Figure 7a. The corresponding Tauc plot (Figure 4b) yielded an indirect band gap of 0.91 eV for $HgCu_3Ti_4O_{12}$. In comparison, $CaCu_3Ti_4O_{12}$ shows two absorption edges in the visible region corresponding to band gaps of approximately 2.21 and 1.39 eV, which enable its activity as a visible-light photocatalyst for the degradation of water pollutants via photo-sensitized oxidation [42]. Notably, the band gap of $HgCu_3Ti_4O_{12}$ is further red-shifted by 0.47 eV relative to the lower band gap (1.39 eV) of $CaCu_3Ti_4O_{12}$. This significant reduction suggests that $HgCu_3Ti_4O_{12}$ may exhibit enhanced light absorption in the visible to near-infrared range, potentially leading to higher photocatalytic efficiency under solar irradiation compared to $CaCu_3Ti_4O_{12}$.

Figure 5a,b present the temperature dependences of the dielectric constant $\varepsilon_r(T)$ and dielectric loss $\delta(T)$ for $HgCu_3Ti_4O_{12}$ measured at selected frequencies over the range of 10 to 300 K. The

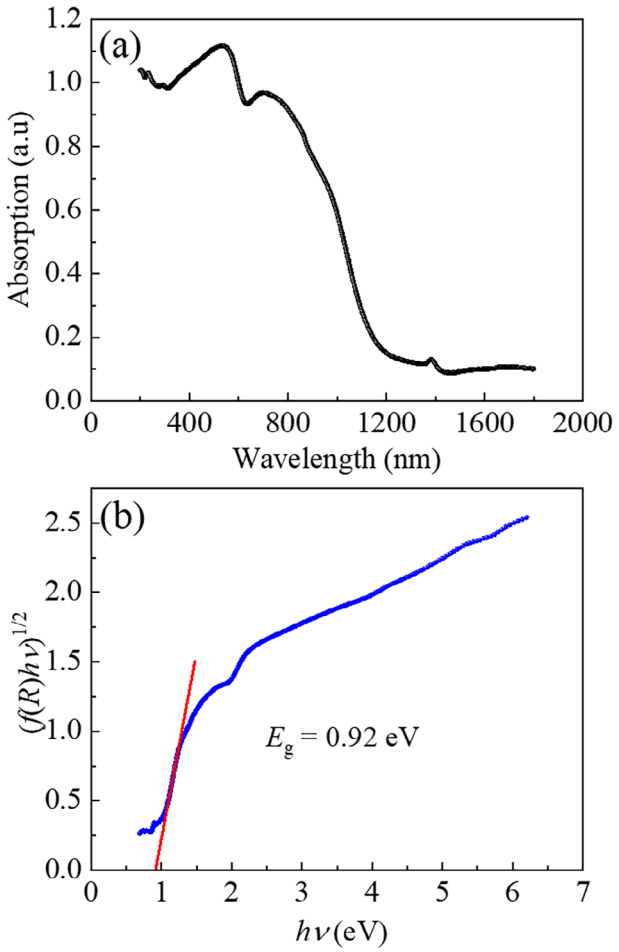

FIGURE 4 | (a) UV–vis–NIR diffuse reflectance spectrum of $HgCu_3Ti_4O_{12}$ measured at room temperature. (b) the Tauc plot obtained on the basis of the equation $(f(R)h\nu)^{1/2} = A(h\nu\text{-}E_g)$ for band gap estimation, where $f(R)$, A, and E_g represent the Kubelka-Munk function, proportional constant, and band gap.

overall shape and trend of the $\varepsilon_r(T)$ and tan $\delta(T)$ curves for $HgCu_3Ti_4O_{12}$ are broadly similar to those of $CaCu_3Ti_4O_{12}$, with both materials exhibiting a rapid rise in dielectric constant as temperature increases and a pronounced dielectric loss peak with strong frequency dispersion between 100 and 200 K. Nevertheless, several distinct features that clearly differ from $CaCu_3Ti_4O_{12}$ are observed in $HgCu_3Ti_4O_{12}$. First, the magnitude of the dielectric constant $\varepsilon_r(T)$ for $HgCu_3Ti_4O_{12}$ is only about 10^2 across the entire temperature range, which is far lower than those of the homologous compounds $CdCu_3Ti_4O_{12}$ ($\varepsilon_r \sim 10^3$–10^4) [43] and $CaCu_3Ti_4O_{12}$ ($\varepsilon_r \sim 10^4$–10^5) [6, 16]. Correspondingly, the dielectric loss of $HgCu_3Ti_4O_{12}$ (δ~0.1) is markedly lower than that of $CaCu_3Ti_4O_{12}$ (δ~2) [34]. $CaCu_3Ti_4O_{12}$ is well known for exhibiting a colossal dielectric constant over a broad frequency and temperature range, and the origin of its giant dielectric response has been extensively investigated. The most widely accepted mechanism for $CaCu_3Ti_4O_{12}$ is the extrinsic internal barrier layer capacitor (IBLC) effect [44]. Previous studies have shown that doping Fe or Mn into $CaCu_3Ti_4O_{12}$ can transform it from an extrinsic colossal dielectric with relatively high dielectric loss ($\delta \sim 2$) into an intrinsic, very-low dielectric loss ($\delta \sim 0.05$), yielding an intrinsic $\varepsilon_r(T)$ value of about 75–100 at low temperatures [33, 34].

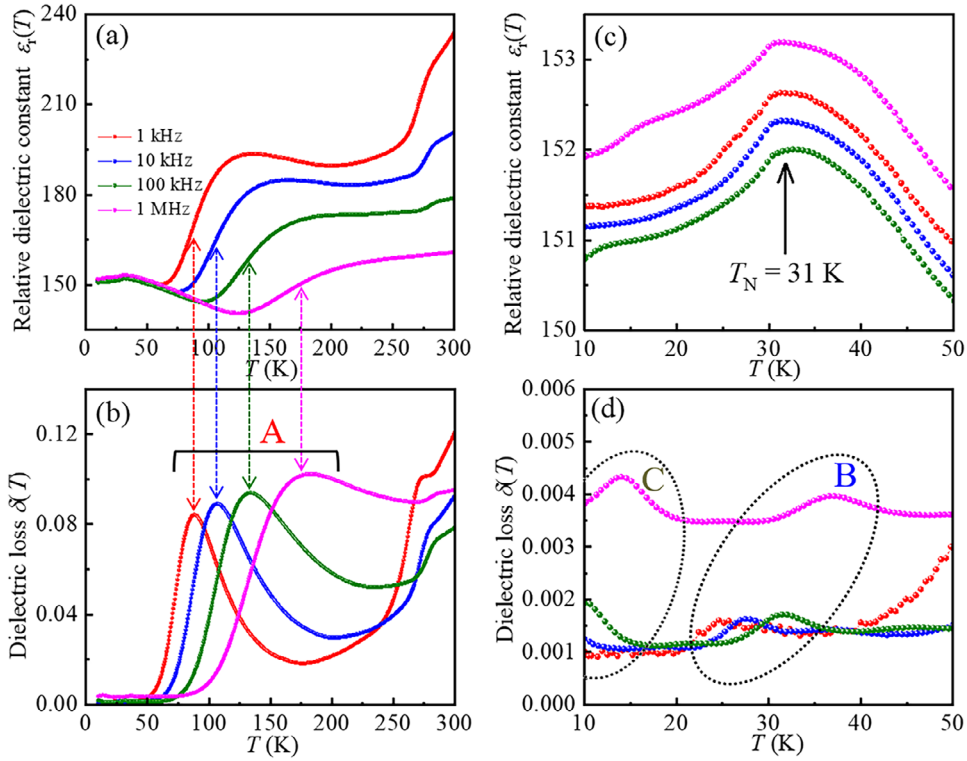

FIGURE 5 | Temperature dependence of (a) relative dielectric constant $\varepsilon_r(T)$, and (b) dielectric loss $\delta(T)$ collected at 1 kHz, 10 kHz, 100 kHz, and 1 MHz for $HgCu_3Ti_4O_{12}$ from 10 to 300 K; (c) and (d) show the enlarged $\varepsilon_r(T)$ and $\delta(T)$ at low temperature range between 10 and 50 K.

In $HgCu_3Ti_4O_{12}$, the dielectric loss is strongly suppressed below 50 K, indicating that dissipative processes are largely frozen out and the measured response approaches the intrinsic dielectric behavior of the material. At 10 K, ε_r reaches approximately 150 with $\delta(T)$ falling below 0.01 (Figure 5d)—values comparable to those reported for Fe- or Mn-doped $CaCu_3Ti_4O_{12}$[33]. This similarity suggests that the dielectric properties of $HgCu_3Ti_4O_{12}$ are intrinsically governed rather than extrinsically dominated. The second characteristic of $HgCu_3Ti_4O_{12}$ is a distinct Debye-type relaxation process, labeled as "A" in Figure 5b. The temperature-dependent dielectric loss curve, particularly in the low-frequency region, displays a nearly symmetric, bell-shaped peak. Especially, the position of this peak aligns precisely with the inflection point of the steepest descent in the $\varepsilon_r(T)$ curve, as indicated by the differently colored arrows. This correspondence reflects the critical frequency at which polarization lag is fully synchronized with the external field—a hallmark of the Debye model characterized by a single relaxation process [34]. Therefore, $HgCu_3Ti_4O_{12}$ offers an ideal platform for investigating Debye-type relaxation. This result was further confirmed by our Arrhenius kinetics analysis as described later. In contrast, previous studies have shown that the dielectric loss peak in $CaCu_3Ti_4O_{12}$ does not coincide with the inflection point of the steepest descent in $\varepsilon_r(T)$ but rather exhibits a notable temperature shift (ΔT) [34]. Such deviation suggests that $CaCu_3Ti_4O_{12}$ does not follow Debye relaxation behavior. In short, it should be noted that, in doped $CaCu_3Ti_4O_{12}$, the reduced dielectric constant and dielectric loss mainly originate from the suppression of extrinsic IBLC or interfacial polarization effects. In contrast, $HgCu_3Ti_4O_{12}$ exhibits a much lower dielectric constant and low dielectric loss without additional doping, suggesting that its dielectric response is less dominated by extrinsic interfacial polarization and is closer to the intrinsic lattice and dipolar responses of the material.

Figure 5c shows enlarged views of $\varepsilon_r(T)$ for $HgCu_3Ti_4O_{12}$ below 50 K. As the temperature decreases, the dielectric constant initially increases gradually, then exhibits a distinct turning point near the AFM transition temperature. Upon further cooling, the dielectric constant begins to decline. This dielectric anomaly is closely associated with the onset of AFM order, suggesting a coupling between the dielectric response and magnetic ordering, which is consistent with a magnetodielectric effect. Such a feature is also observed in Fe, Nb, and Mn-doped $CaCu_3Ti_4O_{12}$ [33, 34]. The origin of the magnetodielectric effect in $HgCu_3Ti_4O_{12}$ may be traced to its distinctive exchange pathway. As mentioned above, direct exchange between Cu^{2+} ions is negligible in this compound, while indirect super-exchange proceeds along the Cu^{2+}-O^{2-}-Ti^{4+}-O^{2-}-Cu^{2+} route dominates the magnetic property [12]. This indirect super-exchange coupling, mediated through Ti^{4+} ions, is noteworthy because Ti^{4+} also governs the electric polarizability within the TiO_6 octahedra. This interpretation is further supported by the dielectric loss behavior. Figure 5d shows enlarged views of the dielectric loss $\delta(T)$ for $HgCu_3Ti_4O_{12}$ below 50 K, where two additional weak but discernible relaxation processes—labeled "B" and "C"—are observed. Such features were not even observed in $CaCu_3Ti_4O_{12}$, which we attribute primarily to the dominance of its extrinsic colossal dielectric response, likely masking any weak relaxation process contribution. As will be discussed below, relaxation process B, occurring near the AFM transition, exhibits a relatively small activation energy and an attempt frequency comparable to the lattice vibration frequency. These features provide a reasonable basis for associating relaxation process B with

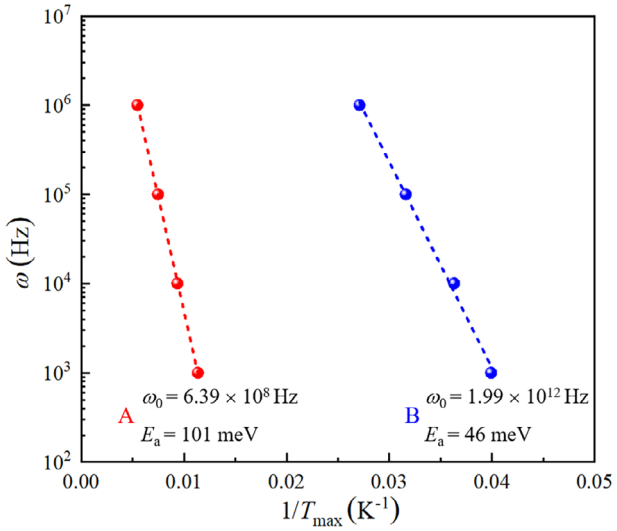

FIGURE 6 | Arrhenius plots for the observed relaxations region A (60–200 K) and B (20–40 K) for $HgCu_3Ti_4O_{12}$.

a collective tilting or "breathing" mode of the TiO_6 octahedron or CuO_4 square plane. Consequently, the Ti^{4+}-mediated magnetic exchange directly couples to the electrical degrees of freedom, offering a credible mechanism for the magnetodielectric coupling observed in $HgCu_3Ti_4O_{12}$.

Arrhenius kinetics provides a foundational framework for analyzing thermally activated dielectric relaxation processes, enabling the quantitative assessment of their temperature-dependent behavior and the extraction of key microscopic activation parameters [34, 45]. Therefore, we employ the Arrhenius law to systematically characterize the distinct relaxation modes identified in $HgCu_3Ti_4O_{12}$, thereby elucidating their underlying physical origins and dynamic signatures. The standard form of the Arrhenius law is given by $\tau = \tau_0 \exp(E_a/k_BT)$, where τ_0 represents the relaxation time at infinite temperature, k_B is the Boltzmann constant, and E_a denotes the activation energy—corresponding to the energy barrier that must be overcome to reorient each polar region. In the present analysis, we employ the equivalent transformed Arrhenius relation, $1/\tau = \omega = \omega_0 \exp(-E_a/k_BT)$, to describe the temperature dependence of the relaxation processes. Figure 6 shows the Arrhenius fitting by using the least-squares method for the two observed relaxation regions A (60–200 K) and B (20–40 K) in $HgCu_3Ti_4O_{12}$. Both processes display excellent linearity with goodness-of-fit (R-factor) values exceeding 0.99. This strong linear correlation indicates that each relaxation process is dominated by a single, well-defined thermally activated mechanism, and the temperature dependence of the relaxation times follows the classical thermal activation law. Consequently, relaxation processes A and B can be regarded as single Debye-type relaxation processes, whose dynamics are governed by distinct energy barriers.

The relaxation process A exhibits an activation energy E_a = 101 meV and $\omega_0 = 6.39 \times 10^8$ Hz. Here, ω_0 is the attempt frequency, which represents the number of times per second that a dipole oscillating near its equilibrium position tries to overcome the energy barrier for a transition. The relatively high activation energy, together with an attempt frequency that is orders of magnitude lower than the typical lattice vibrational frequency (~10^{12}–10^{13} Hz), indicates a reorientation process involving cooperative lattice adjustments rather than a simple localized ion hop. In light of the structural analogy to $CaCu_3Ti_4O_{12}$ and the common occurrence of oxygen vacancies in such perovskite-related oxides, this relaxation can be attributed to the reorientation of oxygen-vacancy–transition-metal defect dipoles [34]. Specifically, oxygen vacancies, which are easily formed during high-pressure synthesis, couple electronically with adjacent reduced cations—most likely Ti^{3+} in TiO_6 octahedra—to form localized electric dipoles. Under an *ac* electric field, these dipoles reorient among symmetry-equivalent directions, overcoming an energy barrier that arises from elastic distortion and electrostatic interactions with the surrounding lattice. The suppressed ω_0 reflects the cooperative nature of the process: the dipole flip is accompanied by a small but coordinated distortion of neighboring TiO_6 units, a characteristic feature of defect-mediated polarization. The relaxation process B is characterized by a much lower activation energy (E_a = 46 meV) and a relatively high attempt frequency ($\omega_0 = 1.99 \times 10^{12}$ Hz), the latter falling within the typical range of optical-phonon frequencies. The very low energy barrier and the lattice-scale attempt frequency point to a highly localized, fast dynamic mode that requires minimal thermal activation. This process can be assigned to low-energy local lattice vibrations of the TiO_6 octahedra or CuO_4 square planes. Especially, in perovskite-type frameworks, TiO_6 octahedra often exhibit collective tilting or breathing modes, some of which may soften under certain temperature and frequency conditions, giving rise to low-energy excitations. The observed activation energy corresponds to the small restoring forces associated with these localized vibrational modes, while the attempt frequency ω_0 directly reflects the intrinsic vibrational frequency of the octahedral units. This relaxation thus represents an intrinsic lattice-dynamic response, essentially decoupled from defect-related polarization. In summary, the dielectric response of $HgCu_3Ti_4O_{12}$ is governed by two different mechanisms: a defect-controlled, slow reorientation process originating from oxygen-vacancy-associated dipoles, and an intrinsic, fast lattice-vibrational mode linked to soft dynamics of TiO_6 octahedra or CuO_4 square-planar. The clear separation of these processes in $HgCu_3Ti_4O_{12}$—unlike the case of $CaCu_3Ti_4O_{12}$, where extrinsic interfacial polarization masks such intrinsic dynamics—highlights the material's more intrinsic dielectric character. These findings provide a coherent microscopic picture of the dielectric relaxation in $HgCu_3Ti_4O_{12}$ and underscore the importance of distinguishing between defect-mediated and lattice-inherent contributions in the design and interpretation of high-permittivity oxides.

Finally, density functional theory (DFT) calculations were performed to understand the physical properties of $HgCu_3Ti_4O_{12}$. Figure 7a presents the calculated electronic structure, which exhibits an insulating ground state with a band gap of 0.9 eV, in good agreement with the optical measurements. The valence and conduction bands are mostly contributed by Cu-3*d* and O-2*p* orbitals. As illustrated in Figure 7b, under the CuO_4 square-planar crystal field, the Cu-3*d* orbitals split into four groups. For the Cu^{2+} ($3d^9$) electronic configuration, one unpaired electron occupies a spin channel of the $d_{x^2-y^2}$ orbital, giving rise to a local magnetic moment of 1 μ_B per Cu ion. The magnetic interactions between

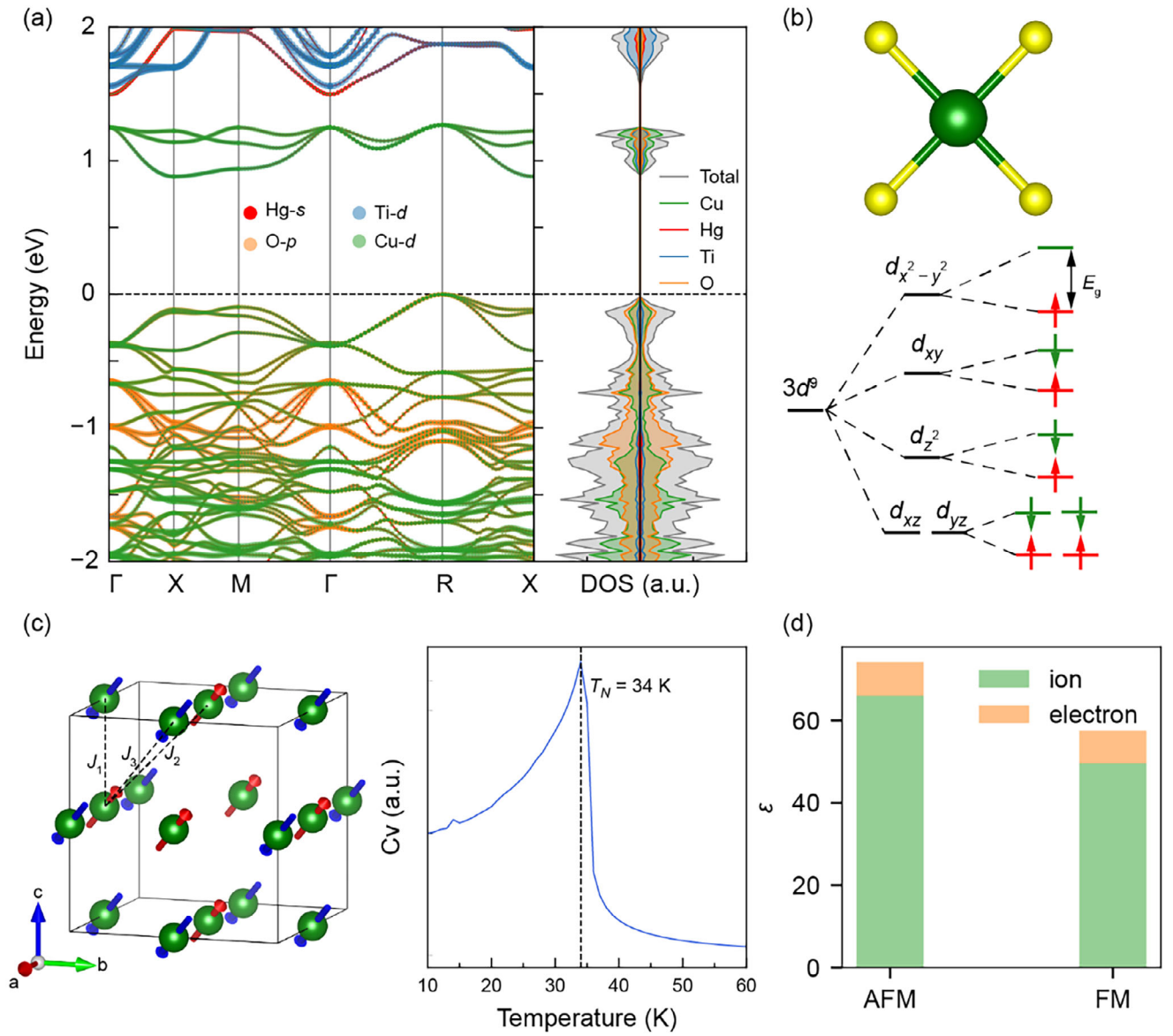

FIGURE 7 | (a) Electronic structure (left panel) and density of states (right panel) of $HgCu_3Ti_4O_{12}$. (b) Square planar geometry of CuO_4 crystal field (upper panel) and the splitting of *d* orbitals (bottom panel). (c) Magnetic structure alongside nearest neighboring interactions and specific heat capacity by Monte Carlo simulations based on the Heisenberg model. (d) Calculated dielectric constant in the antiferromagnetic (AFM) and ferromagnetic (FM) configuration.

Cu atoms can be described by a Heisenberg Hamiltonian:

$$H = -\sum_{ij} J_1 \cdot \vec{S}_i \cdot \vec{S}_j - \sum_{ij} J_2 \cdot \vec{S}_i \cdot \vec{S}_j - \sum_{ij} J_3 \cdot \vec{S}_i \cdot \vec{S}_j$$

where J_i (i = 1/2/3) denotes the ith-nearest-neighbor (NN) exchange interaction between spins $\vec{S}_i$ and $\vec{S}_j$ [left panel of Figure 7c]. The extracted exchange parameters with $S = 1/2$ are $J_1 = -0.71$ meV, $J_2 = 0.47$ meV, and $J_3 = -4.48$ meV, indicating antiferromagnetic coupling for the first- and third-nearest neighbors and ferromagnetic coupling for the second-nearest neighbors. Using these exchange parameters, Monte Carlo simulations based on the Heisenberg model yield an antiferromagnetic transition temperature T_N = 34 K, which is in good agreement with the experimental value shown in Figure 7c. To further prove the coupling between magnetism and dielectric response, we calculated the static dielectric constant ε for both antiferromagnetic and ferromagnetic configurations shown in Figure 7d. The results show that ε_{AFM} is approximately 30% larger than ε_{FM}, providing evidence for magnetodielectric coupling in $HgCu_3Ti_4O_{12}$.

3 | Conclusion

In summary, we have successfully synthesized $HgCu_3Ti_4O_{12}$ under high-pressure. The compound crystallizes in the cubic *Im*-3 structure. Bond-valence-sum calculations and X-ray absorption spectroscopy indicate a charge distribution of $Hg^{2+}Cu^{2+}{}_3Ti^{4+}{}_4O^{2-}{}_{12}$. A key structural finding is the formation of a perfectly regular and undistorted HgO_{12} icosahedron, which represents the highest and most symmetric oxygen

coordination environment reported for Hg^{2+} in mercury-based oxides. Magnetization measurements reveal that $HgCu_3Ti_4O_{12}$ exhibits antiferromagnetic ordering at $T_N = 31$ K, mediated by indirect super-exchange interaction along the Cu^{2+}-O^{2-}-Ti^{4+}-O^{2-}-Cu^{2+} pathway. $HgCu_3Ti_4O_{12}$ exhibits a significantly lower and intrinsic permittivity (~10^2), which is governed by two distinct Debye-type relaxation processes: a high-temperature process (activation energy $E_a = 101$ meV, attempt frequency $\omega_0 = 6.39 \times 10^8$ Hz) associated with the reorientation of oxygen vacancy–defect dipoles, and a low-temperature process ($E_a = 46$ meV, $\omega_0 = 1.99 \times 10^{12}$ Hz) linked to low-energy local lattice vibrations of the TiO_6 octahedra or CuO_4 square planes. A dielectric anomaly around T_N suggests the presence of magnetodielectric coupling, likely by the same super-exchange pathway. Theoretical calculations provide robust support for the experimental findings. DFT calculations reveal that $HgCu_3Ti_4O_{12}$ possesses an insulating ground state with an indirect band gap of 0.9 eV. Monte Carlo simulations based on the Heisenberg model accurately reproduce the antiferromagnetic order and predict a $T_N^{theo.} = 34$ K, in excellent agreement with the experimental value. Crucially, the calculations show that the static dielectric constant in the antiferromagnetic state is approximately 30% larger than that in a ferromagnetic configuration, thus providing evidence for magnetodielectric coupling in $HgCu_3Ti_4O_{12}$. This work not only experimentally clarifies the origin of the magnetodielectric effect in this system but also expands the family of quadruple perovskites, demonstrating how targeted cation chemistry can be employed to tune structural, magnetic, and dielectric functionalities.

4 | Experimental Section

$HgCu_3Ti_4O_{12}$ was prepared by solid-state reactions under high-pressure and high-temperature conditions. The starting materials HgO (99.9% pure, Alfa Aesar), CuO (99.9% pure, Alfa Aesar), and TiO_2 (99.99% pure, Alfa Aesar) were homogenously mixed in the stoichiometric ratio of 1:3:4 and pressed into a pellet. The nominal stoichiometric reaction can be expressed as: $HgO + 3CuO + 4TiO_2 \rightarrow HgCu_3Ti_4O_{12}$. The pre-pressed pellets were wrapped in a gold capsule and then calcined at 1373 K and 5 GPa for 30 min using a cubic-anvil-type high-pressure apparatus [46, 47]. The temperature was quenched to room temperature before pressure was released. After the high-pressure and high-temperature process, the polycrystalline $HgCu_3Ti_4O_{12}$ sample with brown color was obtained.

For phase identification and structure analysis, $HgCu_3Ti_4O_{12}$ was characterized by powder X-ray diffraction (XRD) using a Rigaku diffractometer with a wavelength of 1.5406 Å (Cu K_α radiation, 40 kV, 40 mA). Diffraction data were collected in the angle (2θ) range from 5° to 100° with steps of 0.01°at room temperature. The GSAS program was used to refine the structural parameters with the Rietveld method [48]. The oxidation states of transition metal ions were investigated by soft X-ray absorption spectroscopy (*s*XAS) at the BL11A beamline of the National Synchrotron Radiation Research Center (NSRRC) in Taiwan using the total electron yield (TEY) model. $SrTiO_3$ and CuO were measured simultaneously as a Ti^{4+} reference and a Cu^{2+} reference, respectively. DC magnetic susceptibility was measured by Quantum Design magnetic property measurement system SQUID magnetometer with zero-field-cooling (ZFC) and field-cooling (FC) mode from 2 to 300 K in an external magnetic field of 0.1 T. Hysteresis loops were measured from −7 to 7 T at different temperatures. Specific heat (C_p) data were collected by a pulse relaxation method on a physical property measurement system calorimeter (Quantum Design, PPMS-14 T). The permittivity was measured with different frequencies by using an Agilent-4980A LCR meter on a hard disk-shaped pellet with 4.0 mm in diameter and 300 μm in thickness [3, 9]. Silver paste was applied as electrodes. Diffuse-reflectance spectra were measured at room temperature using a UV–vis–NIR spectrophotometer.

First-principles calculations were performed with the Vienna ab-initio simulation package (VASP) [49, 50]. We adopted the generalized gradient approximation (GGA) in the form of the Perdew–Burke–Ernzerhof (PBE) for the exchange-correlation potentials [51]. The projector augmented-wave (PAW) pseudopotential was used with a plane-wave energy cutoff of 500 eV [52]. A *k*-mesh of 7 × 7 × 7 was used for sampling the first Brillouin zone. Our simulation shows that the spin-orbit coupling effect has a minor influence on the electronic structure, and thus was not considered in the calculations. Atomic positions are relaxed until all the forces on the ions are less than 10^{-2} eV/Å. The self-consistent field procedure was considered converged when the energy difference between two consecutive cycles was lower than 10^{-6} eV. The GGA+U method with Dudarev's approach was applied for *d* orbitals of Cu atoms, where the effective *U* parameter $U_{eff} = U - J = 1.6$ eV was chosen to get a consistent band gap with experiment [53].

Acknowledgements

The work was supported by Beijing Natural Science Foundation (Grant Number 1262041), the National Natural Science Foundation of China (Grant Nos. 12204515, 12425403, 12404005, and 22171283), the National Key Research and Development Program of China (Grant Nos. 2022YFA1403800, 2023YFA1406000, 2024YFA1408000), and Beijing National Laboratory for Condensed Matter Physics (Grant Number 2023BNLCMPKF006). J. F. Z. acknowledges the support of the Young Elite Scientists Sponsorship Program by CAST (Grant Number 2022QNRC001). J. D. was supported by the director's fellowship of HPSTAR. We acknowledge the support from the Max Planck-POSTECH-Hsinchu Center for Complex Phase Materials.

Conflicts of Interest

The authors declare no competing financial interest.

Data Availability Statement

The data that support the findings of this study are available from the corresponding author upon reasonable request.

References

1. C. Q. Jin, J. S. Zhou, J. B. Goodenough, et al., "High-Pressure Synthesis of the Cubic Perovskite $BaRuO_3$ and Evolution of Ferromagnetism in $ARuO_3$ (A = Ca, Sr, Ba) Ruthenates," *Proceedings of the National Academy of Sciences* 105 (2008): 7115–7119.

2. Z. Deng, X. Wang, M. Wang, et al., "Giant Exchange-Bias-like Effect at Low Cooling Fields Induced by Pinned Magnetic Domains in Y_2NiIrO_6 Double Perovskite," *Advanced Materials* 35 (2023): 2209759, https://doi.org/10.1002/adma.202209759.

3. J. Zhao, J. Gao, W. Li, et al., "A Combinatory Ferroelectric Compound Bridging Simple ABO_3 and A-Site-Ordered Qudruple Perovskite," *Nature Communications* 12 (2021): 747.

4. Y. Long and Y. Shimakawa, "Intermetallic Charge Transfer Between A-site Cu and B-site Fe in A-site-ordered Double Perovskites," *New Journal of Physics* 12 (2010): 063029.

5. Y. Shimakawa, "A-Site-Ordered Perovskites with Intriguing Physical Properties," *Inorganic Chemistry* 47 (2008): 8562–8570, https://doi.org/10.1021/ic800696u.

6. A. P. Ramirez, M. A. Subramanian, M. Gardel, et al., "Giant Dielectric Constant Response in a Copper-Titanate," *Solid State Communications* 115 (2000): 217–220, https://doi.org/10.1016/S0038-1098(00)00182-4.

7. I. Yamada, K. Takata, N. Hayashi, et al., "A Perovskite Containing Quadrivalent Iron as a Charge-Disproportionated Ferrimagnet," *Angewandte Chemie International Edition* 47 (2008): 7032–7035, https://doi.org/10.1002/anie.200801482.

8. H. Shiraki, T. Saito, and Y. Shimakawa, "Structural and Magnetic Properties of A -Site-Ordered Perovskites A $Cu_3Sn_4O_{12}$ with A = Ca^{2+}, Sr^{2+}, and Pb^{2+}," *Chemistry of Materials* 20 (2008): 7077–7080, https://doi.org/10.1021/cm8021209.

9. L. Zhou, J. Dai, Y. Chai, et al., "Realization of Large Electric Polarization and Strong Magnetoelectric Coupling in $BiMn_3Cr_4O_{12}$," *Advanced Materials* 29 (2017): 1703435, https://doi.org/10.1002/adma.201703435.

10. R. D. Johnson, L. C. Chapon, D. D. Khalyavin, P. Manuel, P. G. Radaelli, and C. Martin, "Giant Improper Ferroelectricity in the Ferroaxial Magnet $CaMn_7O_{12}$," *Physical Review Letters* 108 (2012): 067201, https://doi.org/10.1103/PhysRevLett.108.067201.

11. M. Sasaki, T. Tashiro, K. Abiko, Y. Kamimura, M. Takesada, and A. Onodera, "Huge Dielectric Properties of $CdCu_3Ti_4O_{12}$ with CCTO Structure," *Ferroelectrics* 415 (2011): 94–100, https://doi.org/10.1080/00150193.2011.577377.

12. D. Mori, M. Shimoi, Y. Kato, et al., "High-Pressure Synthesis, Structure, Dielectric and Magnetic Properties for $SrCu_3Ti_4O_{12}$," *Ferroelectrics* 414 (2011): 180–189.

13. Y. W. Long, T. Saito, M. Mizumaki, A. Agui, and Y. Shimakawa, "Various Valence States of Square-Coordinated Mn in A-Site-Ordered Perovskites," *Journal of the American Chemical Society* 131 (2009): 16244–16247, https://doi.org/10.1021/ja906668c.

14. C. C. Homes, T. Vogt, S. M. Shapiro, S. Wakimoto, M. A. Subramanian, and A. P. Ramirez, "Charge Transfer in the High Dielectric Constant Materials $CaCu_3Ti_4O_{12}$ and $CdCu_3Ti_4O_{12}$," *Physical Review B* 67 (2003): 092106, https://doi.org/10.1103/PhysRevB.67.092106.

15. O. Yanchevskii, O. V'yunov, A. Belous, and L. Kovalenko, "Dielectric Properties of $CaCu_3Ti_4O_{12}$ Ceramics Doped with Aluminium and Fluorine," *Journal of Alloys and Compounds* 874 (2021): 159861, https://doi.org/10.1016/j.jallcom.2021.159861.

16. M. A. Subramanian, D. Li, N. Duan, B. A. Reisner, and A. W. Sleight, "High Dielectric Constant in $ACu_3Ti_4O_{12}$ and $ACu_3Ti_3FeO_{12}$ Phases," *Journal of Solid State Chemistry* 151 (2000): 323–325, https://doi.org/10.1006/jssc.2000.8703.

17. R. Löhnert, H. Bartsch, R. Schmidt, B. Capraro, and J. Töpfer, "Microstructure and Electric Properties of $CaCu_3Ti_4O_{12}$ Multilayer Capacitors," *Journal of the American Ceramic Society* 98 (2015): 141–147.

18. W. Si, E. Cruz, P. Johnson, P. W. Barnes, P. Woodward, and A. Ramirez, "Epitaxial Thin Films of the Giant-Dielectric-Constant Material $CaCu_3Ti_4O_{12}$ Grown by Pulsed-Laser Deposition," *Applied Physics Letters* 81 (2002): 2056–2058, https://doi.org/10.1063/1.1506951.

19. M. Arbatti, X. Shan, and Z. Y. Cheng, "Ceramic–Polymer Composites with High Dielectric Constant," *Advanced Materials* 19 (2007): 1369–1372, https://doi.org/10.1002/adma.200601996.

20. I. Brown, "Maximum Transition Temperatures and Bond Valence Sums in Copper Oxide Superconductors: The influence of Internal Strain," *Physica C: Superconductivity* 169 (1990): 105–106.

21. A. W. Sleight and C. T. Prewitt, "High-pressure $HgTiO_3$ and $HgPbO_3$: Preparation, Characterization, and Structure," *Journal of Solid State Chemistry* 6 (1973): 509–512, https://doi.org/10.1016/S0022-4596(73)80007-6.

22. B. Zhou, S. Qin, T. Ma, et al., "High-Pressure Synthesis of Two Polymorphic $HgMnO_3$ Phases and Distinct Magnetism from 2D to 3D," *Inorganic Chemistry* 59 (2020): 3887–3893.

23. B. Zhou, J. Zhang, X. Ye, et al., "Octahedral Distortion and Displacement-Type Ferroelectricity with Switchable Photovoltaic Effect in a $3d^3$-Electron Perovskite System," *Physical Review Letters* 130 (2023): 146101, https://doi.org/10.1103/PhysRevLett.130.146101.

24. J. F. Zhao, X. Wang, X. Shen, et al., "Magnetic Ordering and Structural Transition in the Ordered Double-Perovskite Pb_2NiMoO_6," *Chemistry of Materials* 34 (2021): 97–106, https://doi.org/10.1021/acs.chemmater.1c02826.

25. K. Chen, Y. Mijiti, S. Agrestini, et al., "Valence State of Pb in Transition Metal Perovskites $PbTMO_3$ (TM = Ti, Ni) Determined from X-Ray Absorption near-Edge Spectroscopy," *Physica Status Solidi (b)* 255 (2018): 1800014.

26. F. M. F. De Groot, J. C. Fuggle, B. T. Thole, and G. A. Sawatzky, "L_2, $_3$ X-ray-absorption Edges of d^0 Compounds: K^+, Ca^{2+}, Sc^{3+}, and Ti^{4+} in O_h (octahedral) Symmetry," *Physical Review B* 41 (1990), 928–937, https://doi.org/10.1103/PhysRevB.41.928.

27. M. W. Haverkort, Z. Hu, A. Tanaka, et al., "Determination of the Orbital Moment and Crystal-Field Splitting in $LaTiO_3$," *Physical Review Letters* 94 (2005): 056401, https://doi.org/10.1103/PhysRevLett.94.056401.

28. C. Chang, T. Koethe, Z. Hu, et al., "*c*-axis Dimer and Its Electronic Breakup: the Insulator-to-Metal Transition in Ti_2O_3," *Physical Review X* 8 (2018): 021004.

29. J. Schlappa, C. F. Chang, Z. Hu, et al., "Resonant Soft X-Ray Scattering from Stepped Surfaces of $SrTiO_3$," *Journal of Physics: Condensed Matter* 24 (2012): 035501.

30. L. Tjeng, C. Chen, and S. Cheong, "Comparative Soft-X-ray Resonant-photoemission Study on $Bi_2Sr_2CaCu_2O_8$, CuO, and Cu_2O," *Physical Review B* 45 (1992): 8205–8208, https://doi.org/10.1103/PhysRevB.45.8205.

31. H. Zhao, D. Lu, X. Wang, et al., "High-Pressure Synthesis of Semiconducting $PbCu_3Mn_4O_{12}$ with near-Room-Temperature Ferrimagnetic Order," *Inorganic Chemistry* 63 (2024): 5924–5930.

32. J. Kumar, R. J. Choudhary, and A. Awasthi, "Quantum Paraelectric Glass State in $SrCu_3Ti_4O_{12}$," *Applied Physics Letters* 104 (2014): 262905, https://doi.org/10.1063/1.4885643.

33. S. Krohns, J. Lu, P. Lunkenheimer, et al., "Correlations of Structural, Magnetic, and Dielectric Properties of Undoped and Doped $CaCu_3Ti_4O_{12}$," *European Physical Journal B* 72 (2009): 173–182.

34. R. K. Grubbs, E. L. Venturini, P. G. Clem, J. J. Richardson, B. A. Tuttle, and G. A. Samara, "Dielectric and Magnetic Properties of Fe- and Nb-Doped $CaCu_3Ti_4O_{12}$," *Physical Review B* 72 (2005): 104111, https://doi.org/10.1103/PhysRevB.72.104111.

35. A. Koitzsch, G. Blumberg, A. Gozar, et al., "Antiferromagnetism in $CaCu_3Ti_4O_{12}$ Studied by Magnetic Raman Spectroscopy," *Physical Review B* 65 (2002): 052406, https://doi.org/10.1103/PhysRevB.65.052406.

36. R. D. Shannon, "Revised Effective Ionic Radii and Systematic Studies of Interatomic Distances in Halides and Chalcogenides," *Acta Crystallographica Section A* 32 (1976): 751–767, https://doi.org/10.1107/S0567739476001551.

37. M. A. Subramanian and A. W. Sleight, "$ACu_3Ti_4O_{12}$ and $ACu_3Ru_4O_{12}$ Perovskites: High Dielectric Constants and Valence Degeneracy," *Solid State Sciences* 4 (2002): 347–351, https://doi.org/10.1016/S1293-2558(01)01262-6.

38. L. Yuan, W. Hu, S. Fang, et al., "CdO-CuO-TiO_2 Ternary Dielectric Systems: Subsolidus Phase Diagram and the Effects of Cu Segregation," *Journal of the European Ceramic Society* 38 (2018): 4978–4985, https://doi.org/10.1016/j.jeurceramsoc.2018.07.038.

39. M. Pires, C. Israel, W. Iwamoto, et al., "Role of Oxygen Vacancies in the Magnetic and Dielectric Properties of the High-Dielectric-Constant System $CaCu_3Ti_4O_{12}$: an Electron-Spin Resonance Study," *Physical Review B* 73 (2006): 224404, https://doi.org/10.1103/PhysRevB.73.224404.

40. J. Q. Yan, J. S. Zhou, J. G. Cheng, et al., "Spin and Orbital Ordering in $Y_{1-X}La_xVO_3$," *Physical Review B* 84 (2011): 214405, https://doi.org/10.1103/PhysRevB.84.214405.

41. R. Kumar, C. V. Tomy, R. Nagarajan, P. L. Paulose, and S. K. Malik, "Magnetization and Heat Capacity Studies of Double Perovskite Compounds Ba_2SmRuO_6 and Ba_2DyRuO_6," *Physica B: Condensed Matter* 404 (2009): 2369–2373, https://doi.org/10.1016/j.physb.2009.04.046.

42. J. H. Clark, M. S. Dyer, R. G. Palgrave, et al., "Visible Light Photo-Oxidation of Model Pollutants Using $CaCu_3Ti_4O_{12}$: an Experimental and Theoretical Study of Optical Properties, Electronic Structure, and Selectivity," *Journal of the American Chemical Society* 133 (2011): 1016–1032.

43. R. Zuo, L. Feng, Y. Yan, B. Chen, and G. Cao, "Observation of Giant Dielectric Constant in $CdCu_3Ti_4O_{12}$ Ceramics," *Solid State Communications* 138 (2006): 91–94, https://doi.org/10.1016/j.ssc.2006.02.002.

44. R. Z. Xue, D. W. Liu, Z. P. Chen, H. Y. Dai, J. Chen, and G. Y. Zhao, "Dielectric and Nonohmic Properties of $CaCu_3Ti_4O_{12}/SrTiO_3$ Ceramics," *Journal of Electronic Materials* 44 (2015): 1088–1094, https://doi.org/10.1007/s11664-015-3645-4.

45. W. Yang, X. Liu, H. Zhao, Y. Lin, and X. Chen, "Structure, Magnetic, and Dielectric Characteristics of Ln_2NiMnO_6 (Ln = Nd and Sm) Ceramics," *Journal of Applied Physics* 112 (2012): 064104, https://doi.org/10.1063/1.4752262.

46. Z. Deng, C. J. Kang, M. Croft, et al., "A Pressure-Induced Inverse Order-Disorder Transition in Double Perovskites," *Angewandte Chemie International Edition* 59 (2020): 8240–8246.

47. J. Zhang, X. Wang, L. Zhou, et al., "A Ferrotoroidic Candidate with Well-Separated Spin Chains," *Advanced Materials* 34 (2022): 2106728, https://doi.org/10.1002/adma.202106728.

48. B. H. Toby, "EXPGUI, a Graphical User Interface for GSAS," *Journal of Applied Crystallography* 34 (2001): 210–213, https://doi.org/10.1107/S0021889801002242.

49. G. Kresse and J. Furthmüller, "Efficiency of Ab-Initio Total Energy Calculations for Metals and Semiconductors Using a Plane-Wave Basis Set," *Computational Materials Science* 6 (1996): 15–50, https://doi.org/10.1016/0927-0256(96)00008-0.

50. G. Kresse and J. Furthmuller, "Efficient Iterative Schemes for Ab Initio Total-Energy Calculations Using a Plane-Wave Basis Set," *Physical Review B* 54 (1996): 11169–11186, https://doi.org/10.1103/PhysRevB.54.11169.

51. P. Perdew, K. Burke, and M. Ernzerhof, "Generalized Gradient Approximation Made Simple," *Physical Review Letter* 78 (1997): 1396.

52. G. Kresse and D. Joubert, "From Ultrasoft Pseudopotentials to the Projector Augmented-Wave Method," *Physical Review B* 59 (1999): 1758–1775, https://doi.org/10.1103/PhysRevB.59.1758.

53. S. L. Dudarev, G. A. Botton, S. Y. Savrasov, C. Humphreys, and A. P. Sutton, "Electron-Energy-Loss Spectra and the Structural Stability of Nickel Oxide: An LSDA+ U Study," *Physical Review B* 57 (1998): 1505.